ARTICLES

Intersubunit coordination in a homomeric ring ATPase

Jeffrey R. Moffitt[1]*, Yann R. Chemla[1]*†, K. Aathavan[2], Shelley Grimes[3], Paul J. Jardine[3], Dwight L. Anderson[3,4] & Carlos Bustamante[1,2,5]

Homomeric ring ATPases perform many vital and varied tasks in the cell, ranging from chromosome segregation to protein degradation. Here we report the direct observation of the intersubunit coordination and step size of such a ring ATPase, the double-stranded-DNA packaging motor in the bacteriophage φ29. Using high-resolution optical tweezers, we find that packaging occurs in increments of 10 base pairs (bp). Statistical analysis of the preceding dwell times reveals that multiple ATPs bind during each dwell, and application of high force reveals that these 10-bp increments are composed of four 2.5-bp steps. These results indicate that the hydrolysis cycles of the individual subunits are highly coordinated by means of a mechanism novel for ring ATPases. Furthermore, a step size that is a non-integer number of base pairs demands new models for motor–DNA interactions.

Multimeric ring ATPases of the ASCE (additional strand, conserved E) superfamily represent a structurally homologous yet functionally diverse group of proteins involved in such varied tasks as ATP synthesis, protein unfolding and degradation, and DNA translocation[1–5]. Despite their importance, the coordination mechanism between the hydrolysis cycles of the individual and often identical subunits that compose these ringed proteins is poorly understood. Recent crystallographic and bulk biochemical studies[2,4] suggest various models of coordination in which subunits act sequentially and in order[6–14], simultaneously and in concert[15], or independently and at random[16]. Unfortunately, direct observation of subunit dynamics has only been reported for a heteromeric system, the F1 ring of ATP synthase[8], the heterodimers of which function in a sequential manner.

The DNA packaging motor in the *Bacillus subtilis* bacteriophage φ29 provides a model system to investigate the intersubunit coordination in homomeric ring ATPases because it can be fully reconstituted *in vitro*[17], it has a relatively slow translocation rate[18,19], and it has been extensively characterized by bulk[20] and single-molecule[18,19,21–23] methods. Packaging of the double-stranded (ds)DNA genome of φ29 into its proteinaceous precursor capsid (prohead) is driven by a powerful molecular machine[18] which consists of three multimeric rings organized coaxially around the point of DNA entry[20]: a dodecameric[24] ring of gene product 10 (gp10) known as the head–tail connector; a pentameric[24–26] ring of RNA molecules known as the prohead-RNA (pRNA); and a pentameric[24,26] ring of the ATPase gp16 (see Fig. 1a). Sequence homology[27] places gp16 in the FtsK/HerA family of dsDNA translocases[28]. This family is itself a member of the large ASCE superfamily, thus relating the packaging motor to the ubiquitous AAA+ and RecA-like proteins[3,5].

Recent studies of the packaging motor have suggested a mechanism in which the subunits operate sequentially[19], each binding ATP, hydrolysing it and translocating the DNA by 2 bp[19,29], before the next subunit repeats this cycle. Although this scheme is consistent with the observed data[19,24,30] and with sequential models proposed for other ring ATPases[2,4,6–14], direct observation of the coordination of the mechanochemical cycles of the individual subunits in the packaging motor is still lacking. Here we report the first measurements of the individual packaging steps of the φ29 motor, which reveal both its step size and the novel coordination between its subunits. Because of its relation to the ASCE superfamily[27], the mechanism for the packaging motor we propose here may have implications for the function of a diverse set of ring ATPases.

DNA is packaged in 10-bp increments

To probe the dynamics of the packaging motor of φ29, single prohead–motor–DNA complexes are tethered between two 860-nm-diameter polystyrene beads held in two optical traps as in Fig. 1a. Packaging is initiated *in situ*[22,23] or by restarting stalled complexes[18,19] in an ATP packaging buffer and monitored in a semi-passive mode in which the tension applied to the motor is kept within a narrow range by periodically changing the distance between the two traps (Supplementary Fig. 1). Motor translocation is determined from the decrease in the contour length of the DNA tether and is followed with base-pair-scale resolution[31–33].

In our first experiments we probe packaging at an average low external tension of ~8 pN, and at ATP concentrations ([ATP]) above and below the Michaelis constant (K_m) of the motor, ~30 μM[19]. Figure 1b shows representative packaging traces collected under these conditions. Across the full range of [ATP], packaging of DNA occurs in a stepwise manner consisting of 'dwells', in which the DNA length remains constant, followed by 'bursts', in which DNA is translocated in ~10-bp increments. We determine the average length of DNA encapsidated in these packaging bursts for each [ATP] from the periodicity in the average pairwise distance distribution (PWD) as seen in Fig. 1c. No statistically significant trend is observed in the size of these bursts as a function of [ATP] (see Fig. 1d); thus, the average of these values, 10.0 ± 0.2 bp (s.e.m.), is the best estimate for the burst size.

To elucidate the mechanism by which the motor translocates in 10-bp increments, we analysed the time the motor spends in the dwell

[1]Department of Physics and Jason L. Choy Laboratory of Single Molecule Biophysics, [2]Biophysics Graduate Group, University of California, Berkeley, California 94720, USA. [3]Department of Diagnostic and Biological Sciences, [4]Department of Microbiology, University of Minnesota, Minneapolis, Minnesota 55455, USA. [5]Departments of Molecular and Cell Biology, Chemistry, and Howard Hughes Medical Institute, University of California, Berkeley, California 94720, USA. †Present address: Department of Physics and Center for Biophysics and Computational Biology, University of Illinois at Urbana-Champaign, Urbana, Illinois 61801, USA.
*These authors contributed equally to this work.

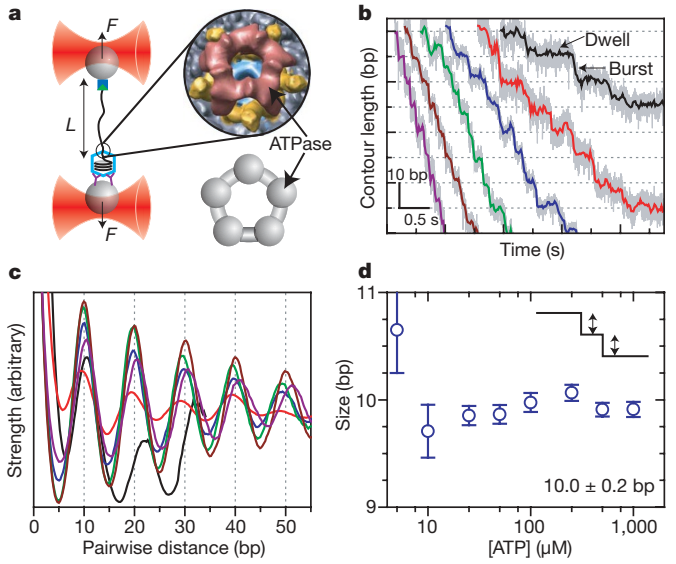

Figure 1 | Bacteriophage φ29 packages DNA in bursts of 10 bp. **a**, A single packaging bacteriophage prohead–motor complex and its dsDNA substrate are tethered between two beads each held in an optical trap and held under tension, *F*. Motor dynamics are inferred from changes in the contour length of the unpackaged DNA, *L*, as a function of time. Inset: cryo-electron microscopy reconstruction of the full motor complex[26] (courtesy of M. Morais), ATPase in red, pRNA in yellow, connector in cyan and capsid in grey with a top view cartoon of the ATPase ring alone (below, grey). **b**, Representative packaging traces collected under low external load, ~8 pN, and different [ATP]: 250 μM, 100 μM, 50 μM, 25 μM, 10 μM and 5 μM in purple, brown, green, blue, red and black, respectively, all boxcar-filtered and decimated to 50 Hz. Data at 1.25 kHz are plotted in light grey. Contour length is plotted in bp of dsDNA. **c**, Average pairwise distributions of packaging traces selected for low noise levels (50% of all packaging data; see Supplementary Figs 2 and 3). Colour scheme as in **b**. **d**, The average size of the packaging burst versus [ATP] determined from the periodicity in **c**. Error bars are the standard deviation in the slope of a linear fit to the peak positions. Data collected at 500 μM and 1 mM [ATP] are not shown in **b** and **c** for clarity.

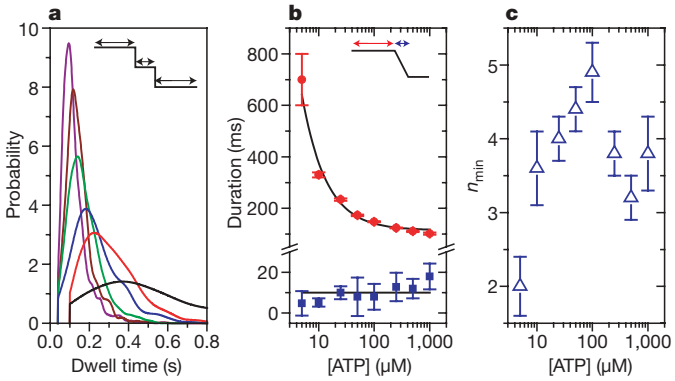

Figure 2 | Dwells before 10-bp bursts contain multiple kinetic events. **a**, Probability distributions for the dwell times preceding a 10-bp burst under low external load, ~8 pN, and different [ATP]: colour scheme as in Fig. 1. Distributions were estimated using kernel density estimation with a Gaussian kernel and the optimum bandwidth[46] and are truncated at the lowest detectable dwell time. Supplementary Fig. 2 contains the number of observed bursts for each [ATP]. Distributions for 500 μM and 1 mM [ATP] are not shown for clarity. **b**, The mean dwell time before the 10-bp bursts (red circles) for all [ATP] with an inverse hyperbolic fit (black line) and the mean duration of all bursts (blue squares, average denoted by black line). **c**, The minimum number of rate-limiting kinetic events during the dwell before the 10-bp bursts, n_{min}, for all [ATP]. Error bars are the standard error.

before each burst and the time it takes to complete each burst as a function of [ATP]. Figure 2a shows the distribution of dwell times before the packaging bursts. The mean dwell time, seen in Fig. 2b, shows a strong dependence on [ATP] that follows an inverse hyperbolic expression, $\langle\tau\rangle = (K_{1/2} + [\mathrm{ATP}])/(k_{max}[\mathrm{ATP}])$, with a $K_{1/2}$ of 23 ± 7 μM (s.d.) and a k_{max} of $8.7 \pm 0.7\ s^{-1}$ (s.d.). In contrast, Fig. 2b shows that the average duration of the packaging burst has little or no dependence on [ATP], suggesting that ATP binding occurs only in the dwells and not in the bursts. Taken together these observations produce a packaging velocity with a Michaelis–Menten [ATP] dependence consistent with previous measurements[19].

The specific shape of the dwell time distributions seen in Fig. 2a provides further information on the kinetic transitions within a single dwell. In particular, the more sharply peaked the distribution, the larger the number of rate-limiting kinetic transitions that compose the dwell[34]. We quantify the degree to which these distributions are peaked with the ratio of the squared mean of the dwell times to their variance, the inverse of the randomness parameter[34] (Fig. 2c). It can be shown that this parameter, n_{min}, provides a strict lower bound[35] on the number of rate-limiting transitions under each [ATP] that occurs during the dwell.

At limiting [ATP], $5\ \mu M \ll K_m$, we measure an n_{min} of 2.0 ± 0.4 (s.e.m), indicating that there are at least two rate-limiting transitions in each dwell. Because ATP binding must be rate limiting under these conditions, we conclude that no less than two ATP molecules bind to the motor before each 10-bp burst. (In contrast, if a single ATP were to bind during each dwell, one would expect the dwell time distribution to be a single exponential and n_{min} to be 1 (refs 34, 36).) At saturating [ATP], $1\ mM \gg K_m$, we measured an n_{min} of 3.8 ± 0.5 (s.e.m.). Because binding is no longer rate limiting, this indicates that at least four non-binding transitions must also occur in each dwell. For intermediate [ATP], both binding and non-binding transitions can be rate limiting; thus, we expect n_{min} to peak to a value greater than either of the extreme values, exactly as is observed. Thus, Fig. 2c indicates that in total no less than six kinetic transitions must occur in the dwell before each 10-bp burst—at least two ATP binding events and at least four non-binding transitions.

Packaging occurs in four 2.5-bp steps

The findings that packaging occurs in 10-bp increments—five times larger than the 2-bp value proposed from bulk measurements[19,29] — and that the preceding dwells contain multiple ATP binding transitions suggest that the 10-bp bursts may be composed of multiple smaller steps that in general may be too fast to resolve under the above conditions. This inference is supported by the observation that many bursts have durations larger than the measurement bandwidth (Figs 1b and 2b), indicative of intermediate kinetic transitions. Supplementary Fig. 4 shows that occasionally these intermediate transitions can be resolved, appearing as short micro-dwells that split the 10-bp burst into smaller steps. A correlation analysis[36] confirms that these smaller steps occur in groups that sum to 10 bp, ruling out the possibility that these events represent a variable burst size (Supplementary Discussion).

As a direct demonstration of the composition of the 10-bp bursts, we follow packaging against high external loads at near-saturating [ATP] (250 μM). Because translocation steps correspond to force-generating kinetic transitions, we expect that the duration of the micro-dwells preceding these steps will increase with increasing external force[37]. Figure 3a shows that, under 40 pN of average load, smaller steps of ~2.5 bp and integer multiples thereof can be clearly and frequently observed. The PWD for this data, shown in Fig. 3b, reveals a periodicity of 2.4 ± 0.1 bp (s.d.) and the step size distribution, shown in Supplementary Fig. 6, has a peak at 2.48 ± 0.03 bp (s.e.m.). The inset to Fig. 3b shows that the periodicity in the PWD is independent of force, indicating that the 2.5-bp step size is a constant feature of the motor and that the 10-bp bursts observed at low force are composed of four 2.5-bp steps. This conclusion is further supported by the prominent fourth peak observed in the PWD which is consistent with the corresponding 10-bp periodicity observed at low force.

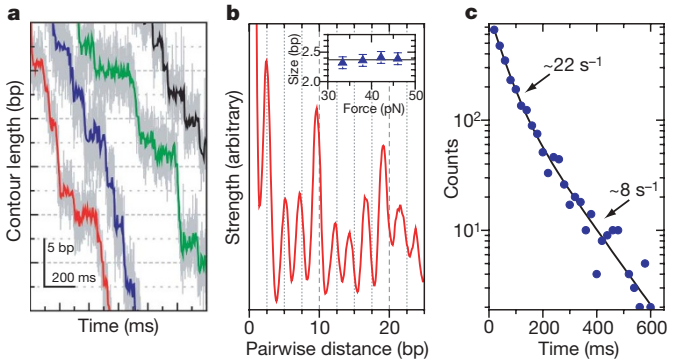

Figure 3 | The 10-bp bursts are composed of four 2.5-bp steps. **a**, Representative packaging traces collected with external loads of ~40 pN and 250 μM [ATP]. Data in light grey are plotted at 1.25 kHz whereas data in colour are boxcar-filtered and decimated to 100 Hz. **b**, Average pairwise distribution of packaging traces selected for low noise levels (50% of all packaging data; see Supplementary Figs 2 and 3). Inset: force dependence of the observed spatial periodicity. The solid line is the mean for all forces, 2.4 ± 0.1 bp (s.e.m.). **c**, Dwell time histogram for the 2.5-bp steps observed under the packaging conditions seen in **a** plotted in blue circles with a bi-exponential fit in black (n = 2,662).

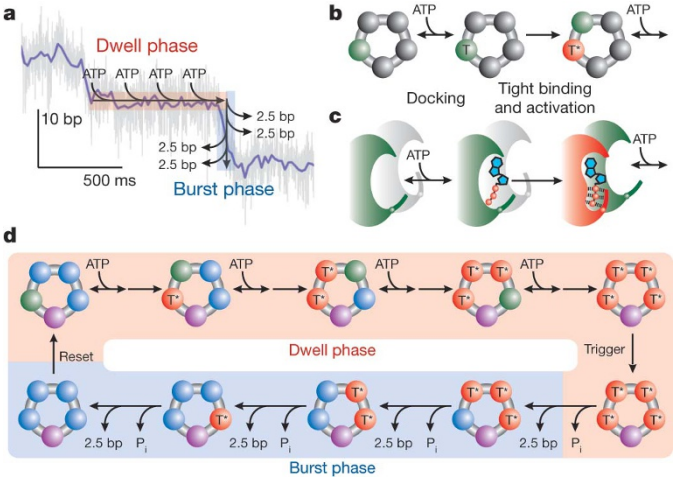

Figure 4 | Intersubunit coordination in the ring ATPase of φ29. **a**, Schematic diagram of the two-phase mechanochemical cycle of φ29 overlaid on a sample packaging trace. **b**, Detailed kinetics of ATP binding. Binding occurs in two steps: ATP docking (green, T) followed by tight binding (red, T*). **c**, Schematic diagram of the communication between subunits during ATP binding. Upon tight binding of an ATP, the binding pocket of the next subunit, formerly inactive (grey), is activated for docking (green). **d**, Schematic depiction of the full mechanochemical cycle of φ29. During the burst phase, ADP may remain on the ring (blue) to be released in the dwell phase. One subunit must be distinct from the others (purple) to break the symmetry of the motor and generate only four steps per cycle. The identity of this subunit may change each cycle. P_i, inorganic phosphate.

The dwell time distribution associated with the 2.5-bp steps (Fig. 3c) is well described by a weighted sum of two exponential decays, with a fast rate of 22 ± 2 s^{-1} (s.d.) and a slow rate of 8 ± 1 s^{-1} (s.d.). The fast rate rationalizes the fraction of 2.5-bp steps that are missed in our analysis and the slow rate is consistent with one out of every four dwells coming from the same peaked dwell time distribution observed at low force (Supplementary Figs 5 and 6). Finally, our data do not support alternative interpretations of the 2.5-bp periodicity, such as distortions from B-form or alternating integer steps, as discussed in Supplementary Figs 7 and 8 and in the Supplementary Information, although some variability in the step size on the ~0.1-bp scale cannot be ruled out.

Intersubunit coordination

Taken together these results indicate that the mechanochemical cycles of the identical subunits of the packaging motor of φ29 are highly coordinated, with the loading of ATP and the translocation of DNA segregated into two distinct phases that comprise the mechanochemical cycle of the entire ring (Fig. 4a). During the dwell phase the DNA is held at constant length while multiple ATPs are loaded, giving this dwell its observed [ATP] dependence (Fig. 2). This process is followed by the burst phase in which DNA is packaged in four increments of 2.5 bp, totalling 10 bp of DNA translocated per cycle (Figs 1d and 3b). Thus, this phase has an average duration that is independent of [ATP] but dependent on force (Fig. 2b).

The observation of four translocation steps per burst strongly suggests that four ATPs bind to the ring during each dwell, one for each of the subsequent steps in the burst phase. This inference is consistent with the measured value of n_{min} at limiting [ATP] as reversibility in binding or differences in binding rates will decrease the observed value of n_{min} from the actual number of binding events[34]. It is also consistent with the 10-bp burst size, as a single ATP provides insufficient free energy to package 10 bp against the high forces tested previously[18,19,37]. Moreover, the binding of four ATPs predicts a coupling constant between ATP consumption and packaging of 2.5 bp per ATP, in reasonable agreement with the ~2 bp per ATP value estimated from bulk measurements[19,29]. The ~25% discrepancy may be explained by additional processes that consume ATP in bulk measurements, such as the repackaging of DNA that slips from the capsid[18,19]. However, it is also possible that a regulatory fifth ATP is bound each cycle and hydrolysed futilely.

Our data also restrict the possible mechanisms by which these ATPs bind to the ring. The requirement that multiple substrate molecules bind per cycle typically results in a sigmoidal dependence on [ATP][38]—the hallmark of binding cooperativity. Yet previous velocity measurements[19] and the mean dwell times measured here (Fig. 2b) are well described by a simple, non-sigmoidal ATP dependence. Because a sigmoidal [ATP] dependence arises whenever two or more binding events are connected reversibly[38], these two observations can be reconciled if and only if the binding of each ATP is separated from the other binding events by a largely irreversible transition. In this case the mean dwell time will display a non-sigmoidal [ATP] dependence despite the cooperative binding of ATP (Supplementary Discussion). This requirement is consistent with previous observations for φ29 (ref. 19) and related ring ATPases[39] which indicate that binding occurs in at least two kinetic steps: (1) a reversible 'docking' transition in which the molecule comes in weak contact with the catalytic pocket; followed by (2) a largely irreversible 'tight-binding' transition[39] in which ATP makes a stronger contact to the binding site and is committed to the hydrolysis cycle (Fig. 4b). More intermediate kinetic states in ATP binding are also possible, but are not required to explain our observations.

In addition, the non-sigmoidal [ATP] dependence of the mean dwell times also restricts the temporal order in which the subunits can dock ATP. Kinetic schemes in which multiple subunits are capable of reversibly docking ATP simultaneously will necessarily have a sigmoidal [ATP] dependence because such schemes have binding events that are reversibly connected[38] (Supplementary Discussion). Thus, it is not sufficient to require that each loose docking of ATP be followed by a tight-binding transition; it is also required that only one subunit at a time can be involved in ATP docking. The simplest model that produces this time-ordered docking is one in which the tight-binding transition of one subunit allosterically activates the binding pocket of another subunit, making it competent to dock ATP, a process depicted in Fig. 4c (Supplementary Discussion). Although our data cannot uniquely determine the actual sequence in which the subunits bind ATP, this required allosteric activation in combination with the known interfacial interactions of adjacent subunits in related ring ATPases[3,5] strongly favours a mechanism in which successive ATP binding occurs in a sequential and ordinal fashion around the ring as depicted in Fig. 4b–d.

Figure 4d summarizes the kinetic transitions that occur during a complete mechanochemical cycle of the packaging motor. During the binding phase, four ATPs bind to the ring in the two-step process depicted in Fig. 4b, c. Previous work has shown that the release of phosphate precedes or coincides with translocation[19]. Thus, after the ring has bound four ATPs, the burst phase is triggered, the first phosphate is released, and the first 2.5-bp step is taken. The burst phase then proceeds with three additional 2.5-bp steps preceded by three force-dependent micro-dwells. The number of rate-limiting steps, n_{min}, at saturating ATP (Fig. 2c) indicates that multiple kinetic transitions in addition to ATP binding must occur during the dwell phase. These transitions may correspond to the hydrolysis of the bound ATPs or the release of multiple ADPs from the previous cycle or, perhaps, both. Moreover, these transitions may occur together either as trigger or reset processes (Fig. 4d) or interspersed between ATP binding events. It is also possible that these additional events correspond to the tight-binding transitions, although this is unlikely given that tight binding is believed to occur quite rapidly[19].

The two-phase model we propose here is also consistent with previous measurements of the packaging motor[18,19]. For example, it has been shown that the binding of a single non-hydrolysable ATP analogue is sufficient to pause the entire motor[19]—a result consistent with the high degree of intersubunit coordination observed here. Furthermore, a biphasic sedimentation profile observed in sucrose gradient experiments suggests the ability of the ring to load multiple nucleotides[19], consistent with our model. Finally, the two-phase model predicts the same dependence of the packaging velocity with force and [ATP] as observed previously[18,19].

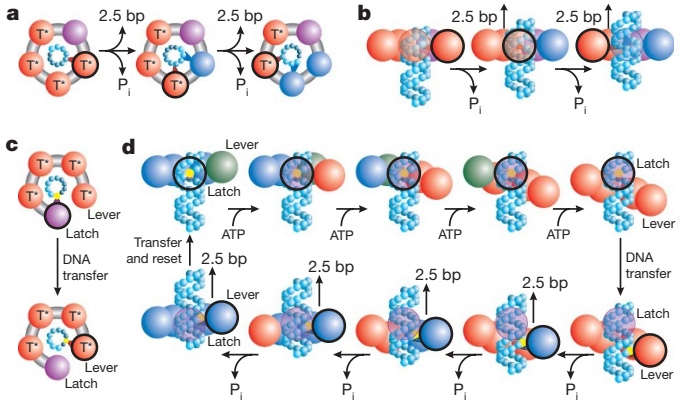

Figure 5 | Packaging models that produce a non-integer step size. **a**, Depiction of a translocation model in which all subunits eventually contact the DNA (cyan spheres). The contacting subunit is outlined in black (top view). **b**, In such a model the size of internal conformational changes set the step size (side view). **c**, Depiction of a translocation model in which only two subunits contact the DNA (black outline). **d**, In such a model, one subunit maintains contact with the DNA (the latch) while the loading of each ATP introduces relative subunit–subunit rotations which distort the ring. This distortion extends one subunit (the lever) along the DNA by ~10 bp. The DNA contact point is then transferred from the latch to the lever, and the release of hydrolysis products relaxes the ring, retracting the lever and the DNA. The DNA contact is then transferred back to the latch, the ring resets and the cycle begins again. Because there are four subunits, the ring is retracted in four steps, dividing a 10-bp step into four ~2.5-bp substeps. The subunit colour scheme is the same as in Fig. 4.

Non-integer step-size models

Our finding that packaging occurs in four 2.5-bp translocation steps raises two notable questions on the motor mechanism. First, how does a dsDNA translocase move in a non-integer number of base pairs? And, second, how is the pentameric symmetry[24–26] of the motor broken, generating only four steps per cycle? A step size that is a non-integer number of base pairs prohibits any mechanism in which every motor subunit within a closed ring makes specific and identical chemical contacts with one strand of the DNA. Under this constraint, we can speculate on several alternative mechanisms that would produce a 2.5-bp step size and the implications these models have for a pentameric motor.

A non-integer step size could be generated if each subunit is capable of binding two or more alternating chemical moieties, which may or may not be on the same strand. Alternatively, the motor may make no specific contacts, but rather drives translocation by means of steric interactions, in which case the step size would be set not by the chemical periodicity of the DNA but by the size of the internal conformational changes that generate the power stroke. One example of such a mechanism is depicted in Fig. 5a, b where each subunit makes non-specific contacts with the major groove of the DNA. In such a model, generation of four translocation steps requires that one of the five subunits is not equivalent to the other four, breaking the symmetry of the pentameric ring. Because the nucleotide-free state is disengaged from the DNA[19], one subunit may be required to retain nucleotide at the end of the previous cycle, ensuring that a strong contact with the DNA is maintained while the remaining subunits load ATP during the subsequent dwell phase.

Alternatively, a single specific chemical contact may be made with the DNA but not with every subunit. In this class of models, only a subset of the subunits interacts with the DNA and relative motion between these subunits is what drives translocation. Figure 5c, d depicts an example of such a mechanism in which only two subunits make specific contact with the DNA. Translocation is achieved via an 'inchworm-like' movement of these two subunits driven by distortions in the ring. One appeal of this mechanism is that because a single specific contact is made with the DNA, it produces an integer burst size, yet because the DNA-binding subunits are retracted by conformational changes induced into the ring by the other subunits, this burst can be divided into non-integer steps. Moreover, this model also explains naturally the observation of four steps by a pentameric motor, as one subunit interface must bear the accumulated distortion of the other four subunits, perhaps inactivating one of the five binding pockets. The relative motion between adjacent subunits needed to accommodate such a mechanism has been observed in the crystal structures of other ring ATPases[6,40] but has not been implicated as part of the translocation mechanism[41]. Future measurements will be aimed at testing the spectrum of models discussed here.

Conclusions

We have presented here the first high-resolution measurements of the stepping dynamics of the ring ATPase of the packaging motor of bacteriophage φ29. Our results indicate a highly coordinated two-phase mechanism in which the binding of ATP and the translocation of DNA by multiple subunits are organized into two distinct and temporally segregated portions of the mechanochemical cycle of the ring. Our observation of a 2.5-bp step size challenges the long-held view that DNA translocation must occur in integer base-pair increments, making it necessary to devise new and more complex models for motor–DNA interactions. In addition, although the inter-subunit coordination we observe is reminiscent of aspects of both the concerted-action model of the large tumour antigen of SV40 (ref. 15) and the sequential models proposed for the translocases BPV E1, T7 gp4, ϕ12 P4, *Escherichia coli* Rho and FtsK[6,7,9–14], our mechanism represents a novel type of coordination not previously proposed for ring ATPases. Provocatively, although a two-phase mechanism contrasts with these other models, it seems to be consistent with many of the biochemical[11–14] and structural[6,7,9,10,13] observations made on these related systems. One notable exception is the ClpX protease for which biochemical data clearly suggest a limited degree of subunit coordination[16]. However, recent work on a related system, the archaeal MCM, suggests that coordinated systems can take alternative pathways when overcoming functional barriers such as catalytically inactive subunits[42]. Ring ATPases of the ASCE superfamily support a large and remarkably diverse set of cellular functions by

drawing on a comparatively small set of common structural features. Direct measurements of the intersubunit dynamics in these systems, such as those presented here, promise to reveal if these diverse cellular functions arise from a similarly small set of common structural dynamics.

METHODS SUMMARY

Complexes of prohead, gp16 and biotinylated DNA were prepared and attached to 860-nm-diameter polystyrene beads (Spherotech) coated with antibodies to φ29 or streptavidin using methods that have been described previously[18,19]. Tethers were assembled and packaging was restarted in a packaging buffer (50 mM Tris-HCl, 50 mM NaCl, 5 mM $MgCl_2$, 10 μg ml^{-1} BSA, 0.1% NaN_3, pH 7.8) supplemented with various amounts of ATP (Sigma-Aldrich)[18,19]. Experiments were conducted in two separate dual-trap instruments, built around two different trapping lasers[32,33], and calibrated using standard techniques[32,33,43]. The contour length of the DNA tether was calculated from the measured force and extension using the extensible worm-like-chain model as described previously[18,19]. Pairwise distributions were calculated from data filtered with a sliding 20-ms boxcar window as described previously[44]. The location and duration of stepping transitions were found with a *t*-test analysis similar to previous methods[45]. Dwell times were calculated directly from the time between transitions, and burst durations were calculated from the number of points within transitions. The mean and variance were calculated directly from these dwell times, and the errors were estimated using a bootstrap method. n_{min} was calculated directly from these moments[34,36].

Full Methods and any associated references are available in the online version of the paper at www.nature.com/nature.

Received 14 May; accepted 11 November 2008.
Published online 7 January 2009.

1. Latterich, M. & Patel, S. The AAA team: related ATPases with diverse functions. *Trends Cell Biol.* **8,** 65–71 (1998).
2. Ogura, T. & Wilkinson, A. J. AAA+ superfamily ATPases: common structure–diverse function. *Genes Cells* **6,** 575–597 (2001).
3. Iyer, L. M., Leipe, D. D., Koonin, E. V. & Aravind, L. Evolutionary history and higher order classification of AAA+ ATPases. *J. Struct. Biol.* **146,** 11–31 (2004).
4. Kainov, D. E., Tuma, R. & Mancini, E. J. Hexameric molecular motors: P4 packaging ATPase unravels the mechanism. *Cell. Mol. Life Sci.* **63,** 1095–1105 (2006).
5. Erzberger, J. P. & Berger, J. M. Evolutionary relationships and structural mechanisms of AAA+ proteins. *Annu. Rev. Biophys. Biomol. Struct.* **35,** 93–114 (2006).
6. Singleton, M. R., Sawaya, M. R., Ellenberger, T. & Wigley, D. B. Crystal structure of T7 gene 4 ring helicase indicates a mechanism for sequential hydrolysis of nucleotides. *Cell* **101,** 589–600 (2000).
7. Mancini, E. J. *et al.* Atomic snapshots of an RNA packaging motor reveal conformational changes linking ATP hydrolysis to RNA translocation. *Cell* **118,** 743–755 (2004).
8. Kinosita, K., Adachi, K. & Itoh, H. Rotation of F1-ATPase: How an ATP-driven molecular machine may work. *Annu. Rev. Biophys. Biomol. Struct.* **33,** 245–268 (2004).
9. Enemark, E. J. & Joshua-Tor, L. Mechanism of DNA translocation in a replicative hexameric helicase. *Nature* **442,** 270–275 (2006).
10. Skordalakes, E. & Berger, J. M. Structural insights into RNA-dependent ring closure and ATPase activation by the Rho termination factor. *Cell* **127,** 553–564 (2006).
11. Adelman, J. L. *et al.* Mechanochemistry of transcription termination factor Rho. *Mol. Cell* **22,** 611–621 (2006).
12. Liao, J.-C., Jeong, Y.-J., Kim, D.-E., Patel, S. S. & Oster, G. Mechanochemistry of T7 DNA helicase. *J. Mol. Biol.* **350,** 452–475 (2005).
13. Massey, T. H., Mercogliano, C. P., Yates, J., Sherratt, D. J. & Löwe, J. Double-stranded DNA translocation: structure and mechanism of hexameric FtsK. *Mol. Cell* **23,** 457–469 (2006).
14. Crampton, D. J., Mukherjee, S. & Richardson, C. C. DNA-induced switch from independent to sequential dTTP hydrolysis in the bacteriophage T7 DNA helicase. *Mol. Cell* **21,** 165–174 (2006).
15. Gai, D., Zhao, R., Li, D., Finkielstein, C. V. & Chen, X. S. Mechanisms of conformational change for a replicative hexameric helicase of SV40 large tumor antigen. *Cell* **119,** 47–60 (2004).
16. Martin, A., Baker, T. A. & Sauer, R. T. Rebuilt AAA+ motors reveal operating principles for ATP-fuelled machines. *Nature* **437,** 1115–1120 (2005).
17. Guo, P., Grimes, S. & Anderson, D. A defined system for *in vitro* packaging of DNA-gp3 of the *Bacillus subtilis* bacteriophage φ29. *Proc. Natl Acad. Sci. USA* **83,** 3505–3509 (1986).
18. Smith, D. E. *et al.* The bacteriophage straight φ29 portal motor can package DNA against a large internal force. *Nature* **413,** 748–752 (2001).
19. Chemla, Y. R. *et al.* Mechanism of force generation of a viral DNA packaging motor. *Cell* **122,** 683–692 (2005).
20. Grimes, S., Jardine, P. J. & Anderson, D. Bacteriophage φ29 DNA packaging. *Adv. Virus Res.* **58,** 255–294 (2002).
21. Hugel, T. *et al.* Experimental test of connector rotation during DNA packaging into bacteriophage φ29 capsids. *PLoS Biol.* **5,** e59 (2007).
22. Fuller, D. N. *et al.* Ionic effects on viral DNA packaging and portal motor function in bacteriophage φ29. *Proc. Natl Acad. Sci. USA* **104,** 11245–11250 (2007).
23. Rickgauer, J. P. *et al.* Portal motor velocity and internal force resisting viral DNA packaging in bacteriophage φ29. *Biophys. J.* **94,** 159–167 (2008).
24. Simpson, A. A. *et al.* Structure of the bacteriophage φ29 DNA packaging motor. *Nature* **408,** 745–750 (2000).
25. Morais, M. C. *et al.* Cryoelectron-microscopy image reconstruction of symmetry mismatches in bacteriophage φ29. *J. Struct. Biol.* **135,** 38–46 (2001).
26. Morais, M. C. *et al.* Defining molecular and domain boundaries in the bacteriophage φ29 DNA packaging motor. *Structure* **16,** 1267–1274 (2008).
27. Burroughs, A. M., Iyer, L. M. & Aravind, L. in *Gene and Protein Evolution* (ed. Volff, J.-N.) 48–65 (Karger, 2007).
28. Iyer, L. M., Makarova, K. S., Koonin, E. V. & Aravind, L. Comparative genomics of the FtsK-HerA superfamily of pumping ATPases: implications for the origins of chromosome segregation, cell division and viral capsid packaging. *Nucleic Acids Res.* **32,** 5260–5279 (2004).
29. Guo, P., Peterson, C. & Anderson, D. Prohead and DNA-gp3-dependent ATPase activity of the DNA packaging protein gp16 of bacteriophage φ29. *J. Mol. Biol.* **197,** 229–236 (1987).
30. Chen, C. & Guo, P. Sequential action of six virus-encoded DNA-packaging RNAs during phage φ29 genomic DNA translocation. *J. Virol.* **71,** 3864–3871 (1997).
31. Moffitt, J. R., Chemla, Y. R., Smith, S. B. & Bustamante, C. Recent advances in optical tweezers. *Annu. Rev. Biochem.* **77,** 205–228 (2008).
32. Moffitt, J. R., Chemla, Y. R., Izhaky, D. & Bustamante, C. Differential detection of dual traps improves the spatial resolution of optical tweezers. *Proc. Natl Acad. Sci. USA* **103,** 9006–9011 (2006).
33. Bustamante, C., Chemla, Y. R. & Moffitt, J. R. in *Single-Molecule Techniques: A Laboratory Manual* (eds Selvin, P. R. & Ha, T.) 297–324 (Cold Spring Harbor Laboratories, 2008).
34. Schnitzer, M. J. & Block, S. M. Statistical kinetics of processive enzymes. *Cold Spring Harb. Symp. Quant. Biol.* **60,** 793–802 (1995).
35. Koza, Z. Maximal force exerted by a molecular motor. *Phys. Rev. E* **65,** 031905 (2002).
36. Chemla, Y. R., Moffitt, J. R. & Bustamante, C. Exact solutions for kinetic models of macromolecular dynamics. *J. Phys. Chem. B* **112,** 6025–6044 (2008).
37. Bustamante, C., Chemla, Y. R., Forde, N. R. & Izhaky, D. Mechanical processes in biochemistry. *Annu. Rev. Biochem.* **73,** 705–748 (2004).
38. Segel, I. H. *Enzyme Kinetics* (John Wiley & Sons, 1975).
39. Oster, G. & Wang, H. Reverse engineering a protein: the mechanochemistry of ATP synthase. *Biochim. Biophys. Acta* **1458,** 482–510 (2000).
40. Skordalakes, E. & Berger, J. M. Structure of the Rho transcription terminator: mechanism of mRNA recognition and helicase loading. *Cell* **114,** 135–146 (2003).
41. Lisal, J. *et al.* Functional visualization of viral molecular motor by hydrogen-deuterium exchange reveals transient states. *Nature Struct. Mol. Biol.* **12,** 460–466 (2005).
42. Moreau, M. J., McGeoch, A. T., Lowe, A. R., Itzhaki, L. S. & Bell, S. D. ATPase site architecture and helicase mechanism of an archaeal MCM. *Mol. Cell* **28,** 304–314 (2007).
43. Berg-Sorensen, K. & Flyvbjerg, H. Power spectrum analysis for optical tweezers. *Rev. Sci. Instrum.* **75,** 594–612 (2004).
44. Block, S. M. & Svoboda, K. Analysis of high resolution recordings of motor movement. *Biophys. J.* **68,** 230–241 (1995).
45. Carter, N. J. & Cross, R. A. Mechanics of the kinesin step. *Nature* **435,** 308–312 (2005).
46. Parzen, E. On estimation of a probability density function and mode. *Ann. Math. Stat.* **33,** 1065–1076 (1962).

Supplementary Information is linked to the online version of the paper at www.nature.com/nature.

Acknowledgements We thank C. L. Hetherington, M. Nollmann and G. Chistol for a critical reading of the manuscript; C. L. Hetherington, A. Politzer, M. Strycharska, M. Kopaczynska and J. Yu for critical discussions; and J. Choy, S. Grill and S. Smith for advice regarding instrumentation. J.R.M. acknowledges the National Science Foundation's Graduate Research Fellowship and Y.R.C. the Burroughs Welcome Fund's Career Awards at the Scientific Interface for funding. This research was supported in part by NIH grants GM-071552, DE-003606 and GM-059604. The content of this paper is solely the responsibility of the authors and does not necessarily represent the official views of the National Institutes of Health.

Author Contributions J.R.M., Y.R.C. and K.A. conducted the experiments and performed the analysis; S.G., P.J.J. and D.L.A. prepared and provided experimental materials; and J.R.M., Y.R.C., K.A., S.G., P.J.J., D.L.A. and C.B. wrote the paper. J.R.M. and Y.R.C. contributed equally to this work.

Author Information Reprints and permissions information is available at www.nature.com/reprints. Correspondence and requests for materials should be addressed to C.B. (carlos@alice.berkeley.edu).

METHODS

Sample preparation. Proheads, gp16 and genomic DNA were isolated as described previously[47]. For a stalled-complex method of initiation[18,19], a ClaI (New England Biolabs) digest of genomic DNA was biotinylated using Klenow exo$^-$ (New England Biolabs) to fill in the overhang with biotinylated nucleotides (Sigma-Aldrich)[18,19]. Preferential packaging of the left end of the genome[20] favours the formation of prohead–motor–DNA complexes with the 6,149-bp fragment of the ClaI digest. Stalled complexes were then bound to antibody beads, made as described previously[18], and introduced into the tweezers with streptavidin-coated beads. For the *in situ* method of initiation[22,23], a 4,277-bp tether PCR amplified from lambda DNA with a biotinylated primer was bound to streptavidin-coated beads, and stalled prohead–motor complexes[22,23] were bound to antibody beads. In both initiation methods, tethers were formed in the tweezers by physically bumping the two beads. The *in situ* initiation method was used for all [ATP] $\geq$ 25 μM as data were in general less noisy and easier to collect; however, a severe drop in tether formation efficiency below 25 μM required the use of the stalled complex method for low [ATP]. All tether lengths were selected to reduce the effect of packaged DNA on motor dynamics[18,23].

Optical trapping instruments. Two different optical trapping instruments were used in these studies[32,33]. All low-force data for 25 μM $\leq$ [ATP] $\leq$ 250 μM were collected using an instrument built around a 845-nm, 200-mW diode laser[32]. All other data were collected using an instrument built around a high-power, diode-pumped, solid-state 1,064-nm laser[33]. Both instruments exploit the correlations in the motion of the two trapped beads with a differential detection technique[32] to achieve base-pair resolution on the second timescale[31–33]. Owing to increased laser absorption at 1,064 nm[48], the high-force data were collected in an 80% deuterium-oxide (D_2O) buffer to avoid heating effects caused by the high laser power needed to provide the large opposing forces. Supplementary Fig. 5 shows that although D_2O alters the kinetics of packaging, it does not change the size of the packaging bursts. In addition, when working with the 1,064-nm trapping laser, an oxygen scavenging system was added (100 μg ml^{-1} glucose oxidase, 20 μg ml^{-1} catalase, 5 mg ml^{-1} dextrose; Sigma-Aldrich) to prevent the formation of the reactive species singlet oxygen.

Calibration. Traps were calibrated using the thermal fluctuations of the trapped beads[43]. The contour length was calculated from the measured extension and force with the extensible worm-like-chain model using a persistence length of 53 nm, a stretch modulus of 1,200 pN[19,49], and an average B-form DNA rise of 3.4 Å bp^{-1} (ref. 50). Distance calibrations were corroborated with video microscopy[33], which was calibrated to 0.3% with two different distance standards (Nikon; Graticules) and confirmed to 1% by measuring the extension of DNA of different lengths, ~1, 2, 3 and 5.6 kb. All packaging experiments were conducted in a semi-passive mode (Supplementary Fig. 1), in which the trap separation was kept constant as packaging proceeded and was changed discretely to keep the tension within a set range: ~6–10 pN for low-force experiments and ~33–46 pN for high-force experiments. All reported data have been corrected for small systematic errors, ~4% (Supplementary Figs 1 and 2), determined from the discrete changes in the trap separation as described in the Supplementary Discussion.

Analysis. The one-sided autocorrelation of a positional histogram of each semi-passive mode segment was used to calculate the pairwise distributions[44]. 0.25-bp bins and 0.1-bp bins were used for the histograms for the low-force and high-force distributions, respectively. Data were selected for low noise and clarity of steps as described in the Supplementary Discussion. The pairwise distributions of the selected data were averaged together to produce the reported distributions. The average spatial periodicity was quantified from the position of the peaks. Subsets of the high force data were analysed to produce the step-size measurement as a function of force.

Stepping transitions were identified using a *t*-test analysis[45] and a probability threshold of observing a given *t*-value of 10^{-4}. Dwell times were calculated from the time between transitions and step sizes were calculated from the difference in mean position between transitions. The reported dwell time distributions in Figs 2a and 3c were selected based on the size of the subsequent step: 8–12 bp and 1.5–4 bp, respectively. Burst durations were estimated from the exponential decay rate of the distribution of the number of contiguous points for which the *t*-value probability was below the 10^{-4} threshold. Because of our limited time resolution, we could not observe the expected peak in this distribution; thus, we report the observed exponential decay, a value less biased by the time resolution than the mean. The effective bandwidth of the *t*-test algorithm was varied to maximize the number of observed steps while minimizing the systematic errors introduced into the moments of the distribution from a finite dead time. By assuming a Poisson distribution, it was determined that this dead time introduces negligible systematic errors in the calculated moments for all reported distributions.

47. Grimes, S. & Anderson, D. The bacteriophage φ29 packaging proteins supercoil the DNA ends. *J. Mol. Biol.* **266,** 901–914 (1997).
48. Kellner, L. The near infra-red absorption spectrum of heavy water. *Proc. R. Soc. Lond. A* **159,** 0410–0415 (1937).
49. Baumann, C. G., Smith, S. B., Bloomfield, V. A. & Bustamante, C. Ionic effects on the elasticity of single DNA molecules. *Proc. Natl Acad. Sci. USA* **94,** 6185–6190 (1997).
50. Yanagi, K., Prive, G. G. & Dickerson, R. E. Analysis of local helix geometry in three B-DNA decamers and eight dodecamers. *J. Mol. Biol.* **217,** 201–214 (1991).